Investigating the Drell-Yan transverse momentum distribution in the color dipole approach

M. A. Betemps,[1,*] M. B. Gay Ducati,[1,†] M. V. T. Machado,[1,2,‡] and J. Raufeisen[3,§]

[1]*Instituto de Física, Universidade Federal do Rio Grande do Sul, Caixa Postal 15051, CEP 91501-970, Porto Alegre, RS, Brazil*
[2]*Instituto de Física e Matemática, Universidade Federal de Pelotas, Caixa Postal 354, CEP 96010-090, Pelotas, RS, Brazil*
[3]*Los Alamos National Laboratory, MS H846, Los Alamos, New Mexico 87545, USA*

We study the influence of unitarity corrections on the Drell-Yan transverse momentum distribution within the color dipole approach. These unitarity corrections are implemented through the multiple scattering Glauber-Mueller approach, which is contrasted with a phenomenological saturation model. The process is analyzed for the center of mass energies of the BNL Relativistic Heavy Ion Collider (RHIC, $\sqrt{s} = 500$ GeV) and of the CERN Large Hadron Collider (LHC, $\sqrt{s} = 14$ TeV). In addition, the results are extrapolated down to current energies of proton-proton collisions, where nonasymptotic corrections to the dipole approach are needed. It is also shown that, in the absence of saturation, the dipole approach can be related to the QCD Compton process.

I. INTRODUCTION

The high energies available in the hadronic reactions at RHIC (BNL Relativistic Heavy Ion Collider) and to be reached at LHC (CERN Large Hadron Collider) will provide better knowledge concerning parton saturation. In such a kinematical region the production of massive lepton pairs in hadronic collisions [Drell-Yan (DY) process [1]] can be used to investigate the high parton density limit, since it is a clean reaction probing the gluon distribution through the QCD Compton process. In particular, the Drell-Yan transverse momentum (p_T) distribution can be expected to be sensitive to saturation effects.

Saturation and nuclear effects are most conveniently described within the color dipole approach [2], which is, in fact, especially suitable for this purpose (see Refs. [3–6] for some applications). The dipole approach is applicable only at high energies, and it is formulated in the target rest frame, where the DY process looks like a bremsstrahlung of a virtual photon decaying into a lepton pair (see Fig. 1). The advantage of this formalism is that the DY cross section can be written in terms of the same color dipole cross section as small-x deep inelastic scattering (DIS). Although diagrammatically no dipole is present in bremsstrahlung, the dipole cross section arises from the interference of the two bremsstrahlung diagrams, see Ref. [7] for a detailed derivation. The cross section for a radiation of a virtual photon from a quark scattering on a nucleon (N) can be written in a factorized form as [2]

$$\frac{d\sigma_{T,L}(qN \rightarrow \gamma^* X)}{d\ln\alpha} = \int d^2 r_\perp |\Psi_{\gamma^* q}^{T,L}(\alpha, r_\perp)|^2 \sigma_{dip}(\alpha r_\perp),$$

$$(1)$$

where σ_{dip} is the same dipole cross section as in DIS, which

should take into account non-perturbative and saturation effects at high energy [3]. The energy dependence of σ_{dip} is not explicitly written out. Here, $r_\perp$ is the photon-quark transverse separation, and the argument of the dipole cross section, $\alpha r_\perp$, is the displacement of the projectile quark in impact parameter space due to the radiation of the virtual photon, different to the DIS case, where the dipole separation is just $r_\perp$. The $\Psi_{\gamma^* q}^{T,L}$ are the light-cone wave functions for radiation of a transversely (T) or longitudinally (L) polarized photon (see e.g. Ref. [7] for explicit expressions). While the light-cone wave functions are calculable in perturbation theory, the dipole cross section can be determined only with input from experimental data.

The goal of this work is to investigate the influence of unitarity corrections on the DY dilepton p_T distribution, describing these unitarity corrections by the multiple scattering Glauber-Mueller approach [8] and including them into the dipole cross section. The results are contrasted with the QCD improved phenomenological saturation model of σ_{dip}, Ref. [9], which quite successfully describes DIS and diffractive DIS data. In lines of a previous work [3], here it is investigated the role of the $\gamma^* q$ wave functions in the p_T
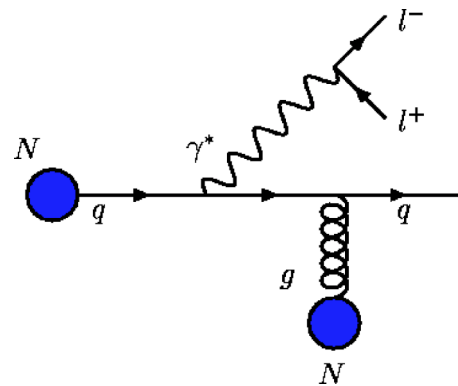

FIG. 1. In the target rest frame, DY dilepton production looks like a bremsstrahlung. A quark or an anti-quark from the projectile hadron scatters off the target color field (denoted by a curly line) and radiates a photon (γ^*) with mass M (before or after the quark scatters), which subsequently decays into the lepton pair ($l^+ l^-$).

*Email address: mandrebe@if.ufrgs.br
†Email address: gay@if.ufrgs.br
‡Email address: magnus@if.ufrgs.br
§Email address: jorgr@lanl.gov

67 114008-1

distribution, characterizing the relation between dipole sizes and transverse momentum. A striking advantage of the color dipole picture is a finite cross section for the lepton pair p_T distribution at small $p_T \to 0$, even in the leading order calculation, feature associated with the saturation encoded in the dipole cross section. In the conventional parton model, the perturbative calculation of $\mathcal{O}(\alpha_s)$ yields a divergence at $p_T = 0$, and one has to resume large logarithms, $\ln(p_T^2/M^2)$, in an appropriated scheme [10], in order to obtain a physically sensible result.

The large amount of low Bjorken-x DIS available data allows to constrain the dipole cross section at very high energies and to calculate the DY cross section without additional free parameters. However, in the current energies of the hadronic colliders there are non-asymptotic corrections to the dipole cross section, which have to be taken into account, in order to describe experimental data. Therefore, one also introduces a parametrization for that contribution, which is negligible already at RHIC energies. In addition, we show how the dipole approach for the DY p_T distribution is related to the QCD Compton process, which contributes at order α_s to the conventional parton model of DY dilepton production. The two approaches are equivalent in a certain limit.

II. RELATING DIPOLE APPROACH AND PARTON MODEL OF HIGH p_T DILEPTON PRODUCTION

Although the dipole approach and the next-to-leading order (NLO) parton model have been compared numerically in Ref. [7], one may still wonder, how these two approaches
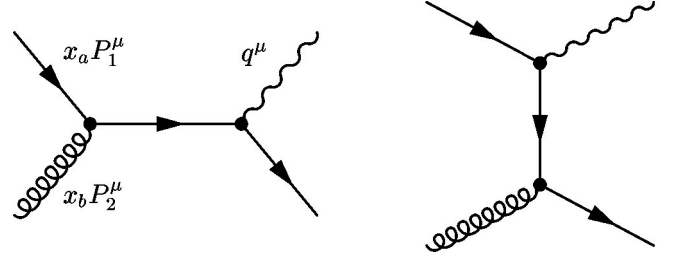

FIG. 2. Production of massive photons through the QCD Compton process. The subsequent decay of the γ^* (wavy line) into the dilepton pair is not shown here. Curly lines denote gluons; quarks are represented by lines with arrows.

can be related to one another analytically. This will be the topic of the present section. Using the leading order expression [11]

$$\sigma_{dip}(x,r_\perp) = \frac{\pi^2 \alpha_s}{3} r_\perp^2 xG(x), \qquad (2)$$

for the dipole cross section, it can be demonstrated how the dipole approach for high p_T dilepton production is related to the QCD Compton process; see Fig. 2. In Eq. (2), $xG(x)$ is the density of gluons with momentum fraction x in a nucleon, and α_s is the strong coupling constant. First, we shortly review the formulas for high p_T dilepton production in the dipole approach and in the parton model, before we show how they can be translated into each other.

In the dipole approach, the DY transverse momentum distribution is given by [12]

$$\frac{d^3\sigma(pp \to l^+l^- X)}{dy\,dM^2\,dp_T^2} = \frac{\alpha_{em}}{3M^2} x_1 \int_{x_1}^{\alpha_{max}} \frac{d\alpha}{\alpha^2} \sum_{q=1}^{N_f} e_q^2 \left[q\left(\frac{x_1}{\alpha}\right) + \bar{q}\left(\frac{x_1}{\alpha}\right) \right] \int d^2r_\perp d^2r'_\perp e^{i\vec{p}_T \cdot (\vec{r}_\perp - \vec{r}'_\perp)} [\Psi^T_{\gamma^* q}(\alpha, r_\perp) \Psi^{T*}_{\gamma^* q}(\alpha, r'_\perp)$$

$$+ \Psi^L_{\gamma^* q}(\alpha, r_\perp) \Psi^{L*}_{\gamma^* q}(\alpha, r'_\perp)] \frac{1}{2} [\sigma_{dip}(x, \alpha r_\perp) + \sigma_{dip}(x, \alpha r'_\perp) - \sigma_{dip}(x, \alpha |\vec{r}_\perp - \vec{r}'_\perp|)], \qquad (3)$$

where the quark (antiquark) distributions in the projectile are denoted by q ($\bar{q}$ respectively). The usual definitions of the kinematic variables are employed, i.e.,

$$x_1 = \frac{2P_2 \cdot q}{s}, \quad x_2 = \frac{2P_1 \cdot q}{s}, \qquad (4)$$

where q is the four momentum of the virtual photon ($M^2 = q^2$), and $P_{1,2}$ are the four momenta of the projectile (1) and target (2) hadron. By evaluating the scalar product for x_1 in the target rest frame, it is easy to show, that the projectile parton distributions in Eq. (3) are probed at momentum fraction x_1/α, where α is the momentum fraction taken by the photon from the projectile quark. Furthermore, p_T is the transverse momentum of the γ^* in a frame with the z-axis parallel to the projectile quark, and

$$y = \frac{1}{2} \ln\left(\frac{x_1}{x_2}\right) \qquad (5)$$

is the rapidity of the photon. In addition,

$$\eta^2 = (1-\alpha)M^2 + \alpha^2 m_q^2. \qquad (6)$$

The quark mass m_q is set to 0 in this section. The upper limit of the α integration in Eq. (3) is determined from the condition that the invariant mass of the final state cannot exceed the total available center of mass (c.m.) energy of the projectile quark-target nucleon system, i.e.,

$$\frac{x_1 s}{\alpha} \geq \frac{p_T^2 + \eta^2}{\alpha(1-\alpha)} \to \alpha_{max} = 1 - \frac{p_T^2}{x_1 s - M^2}, \qquad (7)$$

where $\sqrt{s}$ is the hadronic c.m. energy. In the high energy approximation, $\alpha_{max} = 1$ for $s \rightarrow \infty$. In this section, however, we work with the exact value of α_{max}.

With σ_{dip} given by Eq. (2), the integraldeons over $r_\perp$ and $r'_\perp$ in Eq. (3) can be performed analytically with the result [12]

$$\left(\frac{d^3\sigma(pp \rightarrow l^+ l^- X)}{dy\,dM^2 dp_T^2} \right)_{r_\perp^2 \text{ approx.}}$$

$$= \frac{\alpha_{em}^2 \alpha_s}{9M^2} x_1 \int_{x_1}^{\alpha_{max}} d\alpha \sum_{q=1}^{N_f} e_q^2 \left[q\left(\frac{x_1}{\alpha}\right) + \bar{q}\left(\frac{x_1}{\alpha}\right) \right] xG(x)$$

$$\times \left\{ [1 + (1-\alpha)^2] \frac{p_T^4 + \eta^4}{(p_T^2 + \eta^2)^4} + 4M^2(1-\alpha)^2 \right.$$

$$\left. \times \frac{p_T^2}{(p_T^2 + \eta^2)^4} \right\}. \tag{8}$$

In order to obtain Eq. (8), one has to assume that $xG(x)$ does not depend on $r_\perp$ through scaling violations. Note also, that the $r_\perp^2$ approximation, Eq. (2), is applicable only at large p_T.

In the parton model, on the other hand, the high p_T distribution of DY dileptons produced via the QCD Compton process, see Fig. 2, is given by

$$\left(\frac{d^3\sigma(pp \rightarrow l^+ l^- X)}{dy\,dM^2 dp_T^2} \right)_{\text{Compton}}$$

$$= \frac{\alpha_{em}^2 \alpha_s}{9M^2} \int_{x_a^{min}}^{1} dx_a \frac{x_a x_b}{x_a - x_1} \sum_{q=1}^{N_f} e_q^2 \{ [q(x_a) + \bar{q}(x_a)] G(x_b)$$

$$+ G(x_a)[q(x_b) + \bar{q}(x_b)] \} \frac{1}{\hat{s}^2} \left[-2M^2 \frac{\hat{t}}{\hat{s}\hat{u}} - \frac{\hat{s}}{\hat{u}} - \frac{\hat{u}}{\hat{s}} \right] \tag{9}$$

(see e.g. Ref. [13] for details). In Eq. (9), x_a and x_b are the momentum fractions of the colliding partons, and

$$x_a^{min} = \frac{x_1 - M^2/s}{1 - x_2}. \tag{10}$$

Note that at finite p_T, $x_{a,b} \neq x_{1,2}$, where $x_{1,2} = \sqrt{(p_T^2 + M^2)/s}\, e^{(+,-)y}$. The partonic Mandelstam variables, $\hat{s}$, $\hat{t}$, $\hat{u}$, are defined in terms of x_a, x_b and the four-momenta of the colliding hadrons, see Fig. 2. In order to compare Eqs. (8) and (9), one has to express the partonic Mandelstam variables in terms of α and p_T^2,

$$\hat{s} = (x_a P_1 + x_b P_2)^2 = \frac{p_T^2 + \eta^2}{\alpha(1-\alpha)}, \tag{11}$$

$$\hat{t} = (q - x_b P_2)^2 = -\frac{p_T^2}{1-\alpha}, \tag{12}$$

$$\hat{u} = (q - x_a P_1)^2 = -\frac{p_T^2 + \eta^2}{\alpha}. \tag{13}$$

Furthermore,

$$x_a = \frac{x_1}{\alpha}, \quad x_b = \frac{p_T^2 + \eta^2}{(1-\alpha)p_T^2 + \eta^2} x_2. \tag{14}$$

Inserting the expressions for the partonic Mandelstam variables, Eqs. (11), (12) and (13), into Eq. (9), one obtains a result very similar to Eq. (8), except for the combinations of parton distributions,

$$\left(\frac{d^3\sigma(pp \rightarrow l^+ l^- X)}{dy\,dM^2 dp_T^2} \right)_{\text{Compton}}$$

$$= \frac{\alpha_{em}^2 \alpha_s}{9M^2} x_1 \int_{x_1}^{\alpha_{max}} d\alpha \sum_{q=1}^{N_f} e_q^2 \{ [q(x_a) + \bar{q}(x_a)] x_b G(x_b)$$

$$+ G(x_a) x_b [q(x_b) + \bar{q}(x_b)] \} \left\{ [1 + (1-\alpha)^2] \right.$$

$$\left. \times \frac{p_T^4 + \eta^4}{(p_T^2 + \eta^2)^4} + 4M^2(1-\alpha)^2 \frac{p_T^2}{(p_T^2 + \eta^2)^4} \right\}. \tag{15}$$

When saturation effects are neglected, the dipole approach reproduces that part of the QCD Compton contribution to DY, in which the quark comes from the projectile and the gluon from the target. Thus, the dipole approach is valid, when the first term in the convolution of parton distributions in Eq. (15) dominates. This is the case at large rapidity and at small x_b, both conditions satisfied. The range of validity of the dipole approach can of course only be established *a posteriori*. This is similar to the problem of determining the lowest scale at which perturbative QCD still works. The dipole approach is phenomenologically successful for values of $x_2 < 0.1$, though most parametrizations of the dipole cross section are fitted only to DIS data with Bjorken-$x < 0.01$.

Regarding the rapidity (y) range, in which the dipole formulation can be applied, some guidance on the minimal value of y can be obtained from the numerical comparison of the dipole approach and the next-to-leading order (NLO) parton model in Ref. [7]. At RHIC energy $\sqrt{s} = 500$ GeV, virtually no deviations between the dipole approach and the NLO parton model have been found for $y > 0.5$ [7]. This means that one can safely compare the dipole approach to future DY measurements from the two PHENIX muon arms [14].

On the other hand, the dipole approach takes into account several effects that will be important at high energies. A realistic parametrization of the dipole cross section includes gluon saturation, which is not contained in the standard parton model. Moreover, σ_{dip} contains information about the transverse momentum distribution of the target gluons, thereby is more complete than the gluon distribution in the collinear factorization approach. Finally, with a realistic parametrization of the dipole cross section at large separation
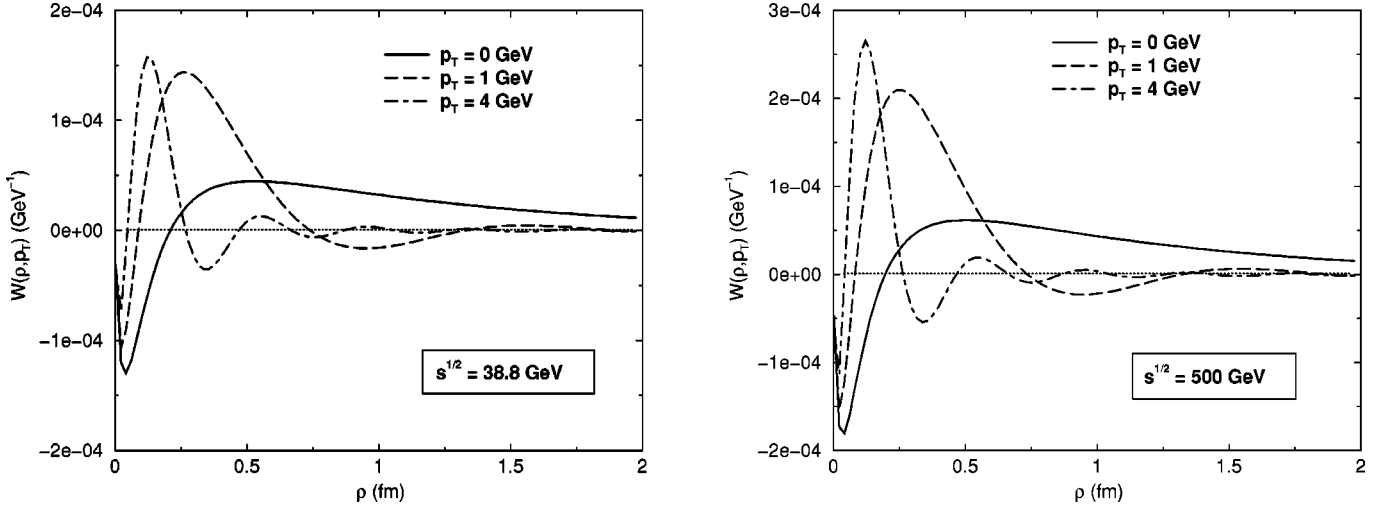
FIG. 3. The weight function $W(\rho, p_T)$ as a function of ρ for different p_T at fixed $x_F = 0.625$ and $M = 6.5$ GeV.

$r_\perp$, one can apply Eq. (3) also at low p_T, while the conventional parton model p_T distribution, Eq. (9), is applicable only at very high $p_T \gtrsim M$.

III. FEATURES OF THE DRELL-YAN CROSS SECTION IN THE COLOR DIPOLE APPROACH

In this section, it is investigated which distances $r_\perp$ in impact parameter space are important for the Drell-Yan p_T distribution. For this purpose, the behavior of the weight function for σ_{dip} as function of $\rho = \alpha r_\perp$ for different values of p_T is studied.

Three of the four Fourier integrals in Eq. (3) can be performed analytically with the result [4],

$$\frac{d\sigma^{DY}}{dM^2 dx_F d^2 p_T} = \frac{\alpha_{\text{em}}^2}{6\pi^3 M^2} \frac{1}{(x_1 + x_2)} \int_0^\infty d\rho W(\rho, p_T) \sigma_{dip}(\rho),$$
(16)

where the weight function $W(\rho, p_T)$ is given by

$$W(\rho, p_T) = \int_{x_1}^1 \frac{d\alpha}{\alpha^2} \frac{x_1}{\alpha} \sum_{q=1}^{N_f} e_q^2 \left[q\left(\frac{x_1}{\alpha}, M^2\right) + \bar{q}\left(\frac{x_1}{\alpha}, M^2\right) \right]$$

$$\times \left\{ [m_q^2 \alpha^4 + 2M^2(1-\alpha)^2] \right.$$

$$\times \left[\frac{1}{p_T^2 + \eta^2} T_1(\rho) - \frac{1}{4\eta} T_2(\rho) \right] + [1 + (1-\alpha)^2]$$

$$\times \left. \left[\frac{\eta p_T}{p_T^2 + \eta^2} T_3(\rho) - \frac{T_1(\rho)}{2} + \frac{\eta}{4} T_2(\rho) \right] \right\},$$
(17)

and the functions T_i read

$$T_1(\rho) = \rho J_0(p_T \rho/\alpha) K_0(\eta \rho/\alpha)/\alpha,$$
(18)

$$T_2(\rho) = \rho^2 J_0(p_T \rho/\alpha) K_1(\eta \rho/\alpha)/\alpha^2,$$
(19)

$$T_3(\rho) = \rho J_1(p_T \rho/\alpha) K_1(\eta \rho/\alpha)/\alpha.$$
(20)

The functions J_0 and J_1 are the first class Bessel functions of order 0 and 1, whereas K_0 and K_1 are the second class modified Bessel functions of order 0 and 1 (MacDonald functions).

It was shown in Ref. [3] that for the (p_T integrated) mass distribution, the wave functions select the small ρ region. Large values of $\rho \gtrsim 2/M$ are exponentiated by the functions $K_{0,1}$. It should be stressed here that large dipole sizes correspond to the nonperturbative sector of the reactions, whereas small size configurations give the perturbative piece.

In the particular case of the dilepton p_T distribution, a different picture is designed. In Fig. 3, we show $W(\rho, p_T)$ as a function of the photon-quark transverse separation ρ for typical fixed lepton pair mass $M = 6.5$ GeV and Feynman-x ($x_F = 0.625$). The results are presented for two center of mass energies: the plot on the left corresponds to $\sqrt{s} = 38.8$ GeV (available at the E772), whereas in the plot on the right, $\sqrt{s} = 500$ GeV (RHIC). For the effective light quark masses, the value $m_q = 0.2$ GeV was used. Three different values for the dilepton transverse momentum were selected, $p_T = 0$, 1 and 4 GeV.

As can be seen from Eq. (17), the oscillating Bessel functions J_i drive the behavior of the $W(\rho, p_T)$ as a function of ρ. The following general picture can be drawn from the plots: for large p_T the large dipole size configurations get suppressed, because $W(\rho, p_T)$ is rapidly oscillating. This suppression mechanism is different from the exponential suppression of large dipole sizes in the case of the p_T integrated cross section, and complicates the numerical calculation of the p_T distribution. On the other hand, as p_T decreases, large ρ configurations become more important. The case $p_T = 0$ is of particular interest, since the weight function $W(\rho, p_T)$ selects very large dipole configurations and such a region is enhanced by increasing the energy. Therefore, the nonperturbative sector of the process should drive the small p_T regime. On the other hand, the large p_T behavior is almost completely dominated by small dipole configurations [15]. These

features are exploited in the next section, where are also discussed the different models that were employed for the dipole cross section.

IV. THE DIPOLE CROSS SECTION

The cross section for a small color dipole scattering on a nucleon can be obtained from perturbative QCD [11]. However, there are large uncertainties stemming from nonperturbative effects (infrared region) as well as from higher order and higher twist corrections. In the leading $\ln(1/x)$ approximation, the dipole interacts with the target through the exchange of a perturbative Balitskiĭ-Fadin-Kuraev-Lipatov (BFKL) Pomeron, described in terms of the ladder diagrams [16]. In the double logarithmic approximation, the BFKL equation [16] agrees with the evolution equation of Dokshitzer, Gribov, Lipatov, Altarelli, and Parisi [17] (DGLAP equation). In this limit, the dipole cross section reads

$$\sigma_{dip}(x,r_\perp) = \frac{\pi^2 \alpha_s}{3} r_\perp^2 x G^{\mathrm{DGLAP}}(x,\tilde{Q}^2), \qquad (21)$$

where $xG^{\mathrm{DGLAP}}(x,\tilde{Q}^2)$ is the usual DGLAP gluon distribution at momentum fraction x and virtuality scale $\tilde{Q}^2 = \lambda/r_\perp^2$. The factor λ appearing in the virtuality scale $\tilde{Q}^2 = \lambda/r_\perp^2$, has been taken as $\lambda = 4$ [3], although same magnitude values are equivalent at leading logarithmic level [18]. The main feature of the dipole cross section above is the color transparency property, i.e., $\sigma_{dip} \sim r_\perp^2$ as $r_\perp \to 0$. At large dipole size, the dipole cross section should match the confinement property $\sigma_{dip} \sim \sigma_0$. Concerning the large transverse separation (non-perturbative sector), our procedure is to freeze the $r_\perp^2$ in Eq. (21) at a suitable scale larger than r_{cut}^2, which corresponds to the initial scale on the gluon density perturbative evolution, $Q_0^2 = 4/r_{\mathrm{cut}}^2$.

At high energies, an additional requirement should be met: the growth of the parton density (mostly gluons) has to be tamed, since an uncontrolled increasing would violate the Froissart-Martin bound, requiring the black disk limit of the target has to be reached at quite small Bjorken x. This feature can be implemented by using the multiple scattering Glauber-Mueller (GM) approach, which reduces the growth of the gluon distribution by eikonalization in impact parameter space [8]. Therefore, one substitutes xG^{DGLAP} in Eq. (21) by the corrected distribution including unitarity effects, xG^{GM}. A more extensive derivation of the GM dipole cross section and the expression of xG^{GM} can be found in the Sec. III of the Ref. [3]. Following previous work [3], one shall use $x=x_2$ as the energy scale in the dipole cross section, since x_2 in DY is the analog of Bjorken-x in DIS. Note that $x = \alpha x_2$ was used in [7], however, the factor α has only a small numerical influence.

Once the dipole cross section is known, one can also calculate the DY differential cross section, Eq. (16) integrated over p_T, and compare it with the available data at small x_2. However, the current data on DY reactions are measured in a kinematical region where x_2 still takes rather large values, that is, $x_2 \simeq 0.1$ at $\sqrt{s} = 38.8$ GeV, where the color dipole

picture reaches the limit of its validity. Therefore, in order to compare the theory with these data, some procedure should be taken to extend the applicability of the dipole cross section at large x_2.

Note, that the dipole cross section Eq. (21) represents the asymptotic gluonic (Pomeron) contribution to the process, and at large x (low energy) a nonasymptotic quarklike content should be included. In the Regge theory language, this means a Reggeon contribution, and therefore, we added the term [3]

$$\sigma_{dip}^{\mathbb{R}} = \sigma_0 r_\perp^2 x^{0.425}(1-x)^3 \qquad (22)$$

to the dipole cross section, Eq. (21).

Using the expression above, good results are obtained in describing the E772 data [19] on mass distribution with a Reggeon overall normalization $\sigma_0 = 8$ [3], reproducing similar results considering the saturation model [15]. Nevertheless, Eq. (22) has a shortcoming when one calculates the dilepton p_T distribution: due to the fact that the weight function, Eq. (17), selects large dipole configurations at small p_T (see discussion in the previous section) the $\sim r_\perp^2$ behavior in the Reggeon dipole cross section produces a non-negligible contribution at small p_T even at RHIC energies. Therefore, Eq. (22) was modified in order to cure this shortcoming and preserve our previous results. The Reggeon contribution now reads

$$\sigma_{dip}^{\mathbb{R}} = \sigma_0 r_\perp^2 x q_{\mathrm{val}}(x,\tilde{Q}^2), \qquad (23)$$

where the quantity q_{val} is the valence quark distribution from the target and a reasonable description of the same E772 data is obtained with a value $\sigma_0 = 7$. The scaling violation from the valence parton distribution takes care of the steep growing on $r_\perp$, which is present in the simple parametrization of Eq. (22), removing the already mentioned shortcoming in the p_T distribution at high energies.

Our main goal here is to investigate the DY p_T distribution, using the GM dipole cross section. However, for sake of comparison, this analysis is contrasted with the phenomenological saturation model of Bartels, Golec-Biernat, and Kowalski (BGBK dipole cross section), Ref. [9], which also includes the features of the dipole cross section discussed above. The model of Ref. [9] is a QCD improved version of the saturation model of Ref. [20]. The new model explicitly includes QCD evolution, and the dipole cross section is given by

$$\sigma_{dip}(x,r_\perp) = \sigma_0 \left\{ 1 - \exp\left(-\frac{\pi^2 r_\perp^2 \alpha_s(\mu^2) x g(x,\mu^2)}{3\sigma_0} \right) \right\}, \qquad (24)$$

where the scale μ^2 is assumed to have the form

$$\mu^2 = \frac{C}{r_\perp^2} + \mu_0^2. \qquad (25)$$

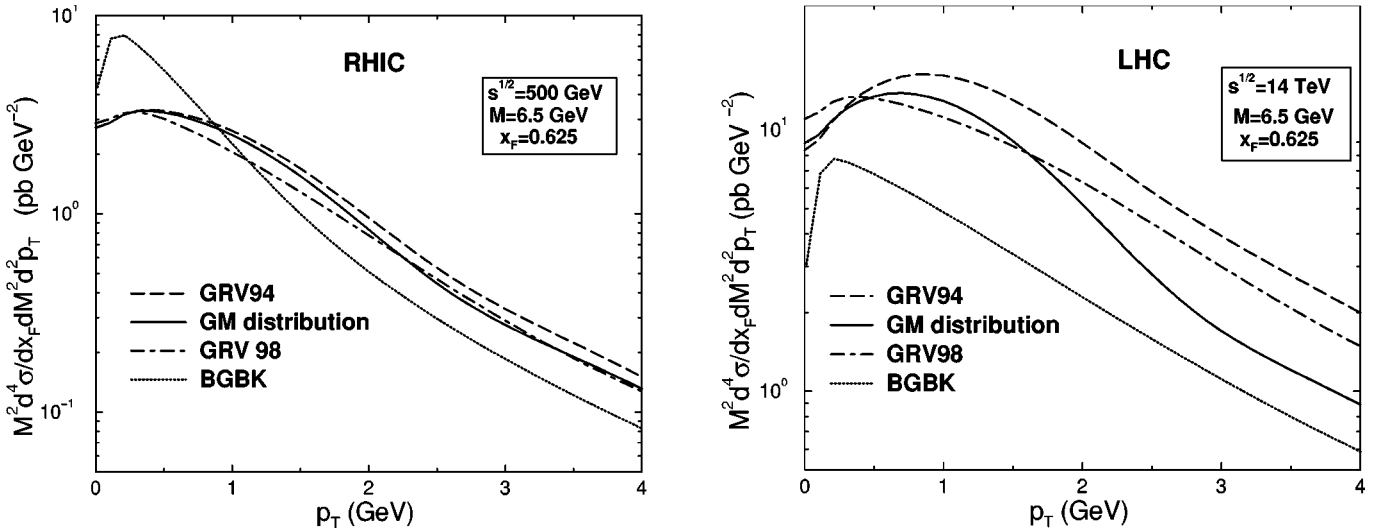The authors of Ref. [9] propose the following gluon distribution at initial scale $Q_0^2 = 1$ GeV^2:

FIG. 4. The Drell-Yan dilepton transverse momentum p_T distribution at RHIC ($\sqrt{s} = 500$ GeV) and LHC ($\sqrt{s} = 14$ TeV). The solid lines are the GM results including unitarity effects; the long-dashed lines are the curves using GRV94 for the gluon distribution (without unitarity effects) in the dipole cross section. The dot-dashed curves are the results obtained with the GRV98 gluon distribution (without unitarity effects) in the dipole cross section and the dotted lines are the results using the BGBK model.

$$xg(x, Q_0^2) = A_g x^{-\lambda_g} (1-x)^{5.6}. \qquad (26)$$

Altogether, there are five free parameters (σ_0, C, μ_0^2, A_g and λ_g), which have been determined in Ref. [9] by fitting ZEUS, H1 and E665 data with $x < 0.01$. In this fit the parameter σ_0 is fixed at 23 mb during the fits as in the original model, Ref. [20]. Here, we employ fit 1 of Ref. [9].

In Ref. [7], where the old saturation model of Ref. [20] was used, the dipole approach was extrapolated to larger x_2 by introducing a threshold factor into the saturation scale, i.e. $Q_s^2 \to Q_s^2 (1-x_2)^5$. The factor $(1-x_2)^5$ is motivated from QCD counting rules and suppresses the large x_2 contribution in the DY cross section. In our case, employing the GM or the BGBK dipole cross section, the large x_2 threshold factor is already included in the collinear gluon distribution function.

In addition, in Ref. [7], $(1-x_1)M^2$ was used as the virtuality scale, at which the projectile parton distribution is probed, see Eq. (16). In this work, we shall use M^2 instead. The factor $(1-x_1)$ is important only at large x_1, but has no effect at midrapidity. In the next section we study the dilepton transverse momentum distribution, making use of the results obtained above for low energies.

V. THE DILEPTON TRANSVERSE MOMENTUM DISTRIBUTION

In this section, the DY dilepton transverse momentum distribution is calculated, using the Glauber-Mueller dipole cross section, Eq. (21), and compared with the results obtained with the improved saturation model, Eq. (24). We will consider typical values for mass and x_F. The projectile structure function employed was the leading order (LO) Glück-Reya-Vogt 1998 (GRV98) parametrization [21] to the GM predictions and CTEQ5L [22] for the saturation model ones.

Before doing that, some comments are in order. The

unitarity effects in the target will be significative at large rapidity $y = 1/2 \ln(x_F/x_2 + 1)$. In the central rapidity region ($y \simeq 0$) the effects in the projectile could be also sizeable. In the last case, those effects in the quark distribution are smaller than in the gluon content. Therefore they will be disregarded in what follows.

In Fig. 4 results for the energies from RHIC ($\sqrt{s} = 500$ GeV) and LHC ($\sqrt{s} = 14$ TeV) are shown with $M = 6.5$ GeV and $x_F = 0.625$. At these energies and kinematics variables, the valence content is completely negligible. We emphasize that the x_F value considered above, is an extreme case, where the rapidity variable acquires large values for RHIC ($y \sim 3$) and LHC ($y \sim 7$) energies. In order to investigate the unitarity effects for this observable, the following comparisons are performed: The long-dashed curves are calculated with the dipole cross section, Eq. (21), without unitarity effects (denoted GRV94) using the GRV94 LO parametrization [23] in calculating the dipole cross section. The solid curves are the result including unitarity effects with the same GRV94 parametrization as initial input. The use of this parametrization is justified properly in Refs. [3,24]. The dot-dashed curves are calculated with the dipole cross section, Eq. (21), using as input the GRV98 parametrization for the gluon structure function. The aim of this comparison is to verify to what extent an updated parametrization can absorb unitarity effects. It is verified that at RHIC energy, the unitarity effects could be absorbed in the parametrization. However, at LHC energy the situation is quite different, and the results are completely distinct. The deviation is important mostly at large p_T, and as a general feature concerning the unitarity effects, those corrections are significant at large transverse momenta and are enhanced as the energy increases.

As an additional comparison, we present curves from the improved saturation model, Eq. (24) (dotted lines in Fig. 4): at RHIC energies and quite small p_T, BGBK results
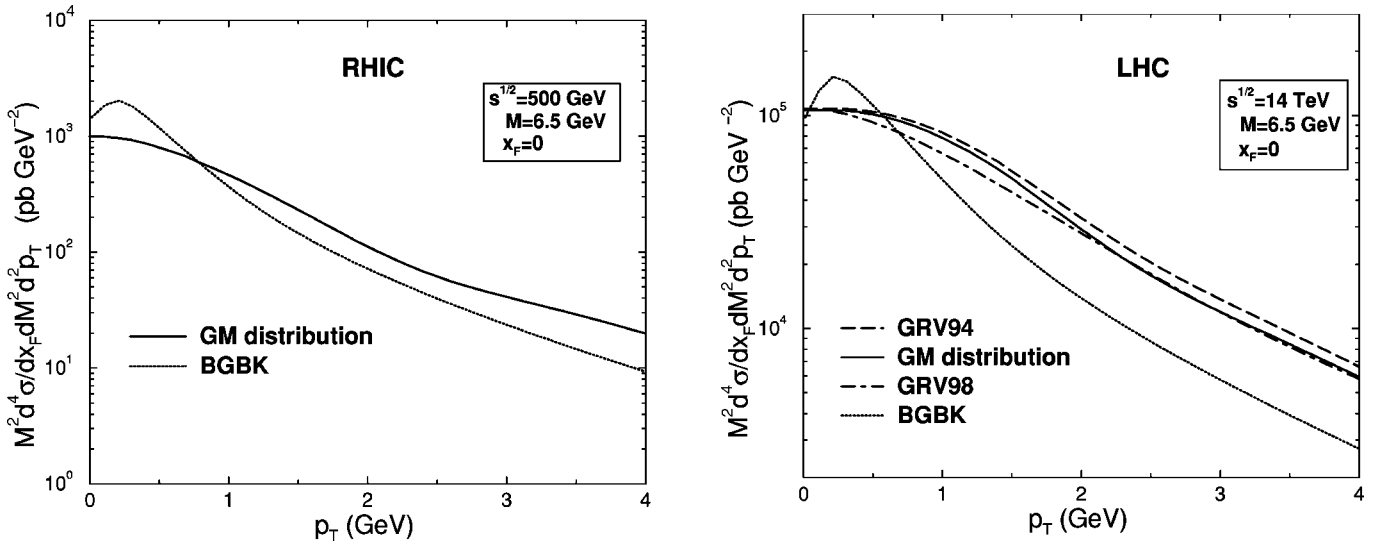
FIG. 5. The Drell-Yan dilepton transverse momentum p_T distribution at RHIC ($\sqrt{s}=500$ GeV) and LHC ($\sqrt{s}=14$ TeV). The curves have the same meaning as in Fig. 4. At RHIC energy, only the GM and BGBK results are shown.

overestimates the GM one; however, at high p_T the BGBK model underestimates the GM predictions. At LHC energies, the BGBK underestimates the GM results. It is worth mentioning that until here the analysis has been performed for fixed values of mass and x_F, which implies that the values of the variable x_2 remain almost unchanged in the analyzed p_T interval. The unitarity effects studied here are calculated perturbatively, and thus they are more significant at small r. At small p_T, large r contributions are important and even dominate in that region, which does not allow to observe the saturation effects in a clear way. There, the confinement aspects of the process are more important. In contrast, at large p_T the main contribution comes from the small r region, which is sensible to the inclusion of unitarity corrections to the process.

In order to perform estimates for more realistic values of the kinematical variables, one considers that the DY measurements at these colliders will be made predominantly in the central rapidity region [25], i.e. at $x_F=0$, instead of a very forward direction. In Fig. 5, we present estimates for RHIC and LHC energies at $x_F=0$. For RHIC, the results for the BGBK model (dotted line) and for the GM approach (solid line) are shown, where the deviations are larger at small p_T. For $x_F=0$, the deviations due to the unitarity effects are smaller than for $x_F=0.625$, so only the GM distribution is shown, since the results with the GRV94 and GRV98 are almost the same as the one with the GM distribution. The results for LHC are also presented. The unitarity effects are smaller at $x_F=0$, because x_2 is larger at midrapidity than in the forward direction.

As a final investigation, the x_F-integrated dilepton transverse momentum distribution is calculated and compared with the available data on pp reactions at $\sqrt{s}=62$ GeV and mass interval $5\leq M\leq 8$ GeV (CERN R209) [26]. The results are presented in Fig. 6, with the solid curve denoting the Glauber-Mueller calculation, including the nonasymptotic valence content (GM+Reggeon), the dot-dashed line is the BGBK result [9] and the long-dashed line is the

Glauber-Mueller calculation without nonasymptotic valence content (GM no Reggeon). The calculation using the improved saturation model shows only fair agreement with the experimental CERN data. Note however, that no Reggeon part has been introduced for the BGBK model. In addition, the data shown in Fig. 6 were integrated over all x_F and therefore include contributions that are not taken into account by the dipole approach (see discussion in Sec. II). The GM result, on the other hand, is in good agreement with the overall normalization and behavior presented by the data, when the nonasymptotic contribution is taken into account, even though no parameters have been adjusted to fit the data. The GM cross section overestimates the saturation model due to the inclusion of the nonasymptotic contribution.
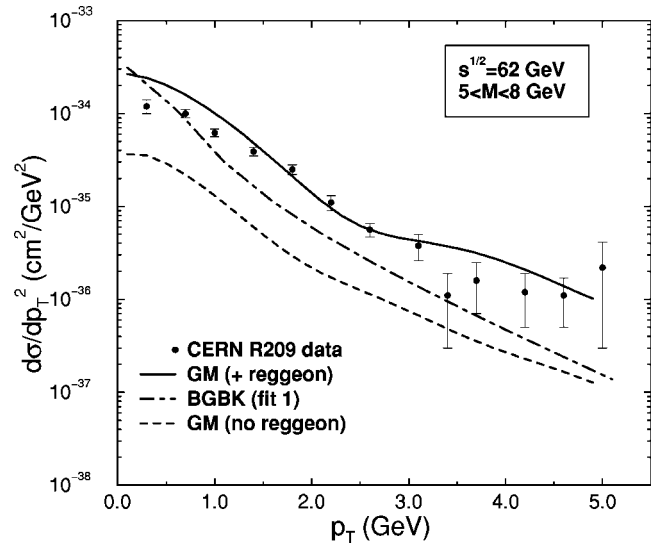

FIG. 6. The Drell-Yan differential cross section on p_T at energy $\sqrt{s}=62$ GeV. The solid line is the GM result and the dot-dashed line is the results using the BGBK model (without Reggeon part). The long-dashed line is the GM results without Reggeon contribution.

VI. CONCLUSIONS

In this work, we investigated in detail the Drell-Yan transverse momentum distribution in the color dipole framework, and we analytically demonstrated that the dipole approach correctly reproduces partially the NLO parton model in the appropriate limit. In contrast with the cross section integrated over p_T, the DY p_T distribution opens a kinematical window where even large dipole configurations contribute. This can be verified by studying the weight function associated with the light cone wave functions for the process for different values of transverse momentum. Large partonic configurations have their maximal contribution at $p_T = 0$. A remarkable feature of the dipole approach is the finite and well behaved property of the dilepton p_T distribution at $p_T \rightarrow 0$ in a LO calculation.

The main motivation to pursue the dipole approach is that it provides a natural framework for the description of unitarity effects, that are not taken into account by the conventional parton model. Unitarity corrections are implemented in the dipole cross section, using the GM approach [8]. In addition, it is performed a comparison with the QCD improved saturation model of the dipole cross section [9]. In general, the unitarity corrections produce a reduction in the differential cross section, mostly at large p_T. At LHC energies, the corrections are quite large and they cannot be reproduced by only using new adjustable parametrizations for the gluon distribution.

In order to extrapolate the dipole approach to lower energies, a Reggeon contribution was introduced into the dipole cross section. This Reggeon part is proportional to the valence quark content of the target, meaning at high energies, i.e. RHIC and LHC, it is negligible, although it is important in order to obtain a good description of the CERN ISR data [26].

[1] S.D. Drell and T.M. Yan, Phys. Rev. Lett. **25**, 316 (1970).

[2] B.Z. Kopeliovich, in *Proceedings*, *Workshop Hirschegg'95: Dynamical Properties of Hadrons in Nuclear Matter*, edited by H. Feldmeier and W. Nörenberg (GSI, Darmstadt, 1995), p. 102, hep-ph/9609385; S.J. Brodsky, A. Hebecker, and E. Quack, Phys. Rev. D **55**, 2584 (1997).

[3] M.A. Betemps, M.B. Gay Ducati, and M.V.T. Machado, Phys. Rev. D **66**, 014018 (2002); in *Proceedings*, *8th International Workshop on Hadron Physics 2002*: *Topics on the Structure and Interaction of Hadronic Systems* (Bento Gonçalves, Brazil, 2002), p. 405.

[4] B.Z. Kopeliovich, J. Raufeisen, A.V. Tarasov, and M.B. Johnson, Phys. Rev. C **67**, 014903 (2003).

[5] M.B. Johnson, B.Z. Kopeliovich, and A.V. Tarasov, Phys. Rev. C **63**, 035203 (2001); J. Raufeisen, Phys. Lett. B **557**, 184 (2003).

[6] F. Gelis and J. Jalilian-Marian, Phys. Rev. D **67**, 074019 (2003).

[7] J. Raufeisen, J.C. Peng, and G.C. Nayak, Phys. Rev. D **66**, 034024 (2002).

[8] A.L. Ayala, M.B. Gay Ducati, and E.M. Levin, Nucl. Phys. **B493**, 305 (1997); **B511**, 355 (1998); M.B. Gay Ducati and V.P. Gonçalves, *ibid.* **B557**, 296 (1999); Nucl. Phys. B (Proc. Suppl.) **79**, 302 (1999).

[9] J. Bartels, K. Golec-Biernat, and H. Kowalski, Phys. Rev. D **66**, 014001 (2002).

[10] J.C. Collins, D.E. Soper, and G. Sterman, Nucl. Phys. **B250**, 199 (1985).

[11] B. Blättel, G. Baym, L.L. Frankfurt, and M. Strikman, Phys. Rev. Lett. **70**, 896 (1993); L. Frankfurt, A. Radyushkin, and M. Strikman, Phys. Rev. D **55**, 98 (1997).

[12] B.Z. Kopeliovich, A. Schäfer, and A. Tarasov, Phys. Rev. C **59**, 1609 (1999).

[13] R. D. Field, *Applications of Perturbative QCD* (Perseus Books, Reading, MA, 1989).

[14] PHENIX Collaboration, W.A. Zajc *et al.*, Nucl. Phys. **A698**, 39 (2002).

[15] B.Z. Kopeliovich, J. Raufeisen, and A.V. Tarasov, Phys. Lett. B **503**, 91 (2001).

[16] E.A. Kuraev, L.N. Lipatov, and V.S. Fadin, Phys. Lett. **60B**, 50 (1975); Sov. Phys. JETP **44**, 443 (1976); **45**, 199 (1977); Ya. Balitsky and L.N. Lipatov, Sov. J. Nucl. Phys. **28**, 822 (1978).

[17] Yu.L. Dokshitzer, Sov. Phys. JETP **46**, 641 (1977); G. Altarelli and G. Parisi, Nucl. Phys. **B126**, 298 (1977); V.N. Gribov and L.N. Lipatov, Sov. J. Nucl. Phys. **28**, 822 (1978).

[18] M. McDermott *et al.*, Eur. Phys. J. C **16**, 641 (2000); L. Frankfurt, M. McDermott, and M. Strikman, J. High Energy Phys. **03**, 45 (2001).

[19] E772 Collaboration, P.L. McGaughey *et al.*, Phys. Rev. D **50**, 3038 (1994); **60**, 119903(E) (1994).

[20] K. Golec-Biernat and M. Wüsthoff, Phys. Rev. D **59**, 014017 (1999); **60**, 114023 (1999).

[21] M. Glück, E. Reya, and A. Vogt, Eur. Phys. J. C **5**, 461 (1998).

[22] CTEQ Collaboration, H.L. Lai *et al.*, Eur. Phys. J. C **12**, 375 (2000).

[23] M. Glück, E. Reya, and A. Vogt, Z. Phys. C **67**, 433 (1995).

[24] M.B. Gay Ducati and M.V.T. Machado, Phys. Rev. D **65**, 114019 (2002).

[25] C. Pajares, Acta Phys. Pol. B **30**, 2263 (1999).

[26] D. Antreasyan *et al.*, Phys. Rev. Lett. **48**, 302 (1982).